# A Cohesive Zone Model to Predict Dynamic Tearing of Rubber

**REFERENCE:** Li, B., and Hoo Fatt, M. S., "A Cohesive Zone Model to Predict Dynamic Tearing of Rubber," *Tire Science and Technology*, TSTCA, Vol. 43, No. 4, October–December 2015, pp. 297–324.

ABSTRACT: Tire failures, such as tread separation and sidewall zipper fracture, occur when internal flaws (cracks) nucleate and grow to a critical size as result of fatigue or cyclic loading. Sudden and catastrophic rupture takes place at this critical crack size because the strain energy release rate exceeds the tear energy of the rubber in the tire. The above-mentioned tire failures can lead to loss of vehicle stability and control, and it is important to develop predictive models and computational tools that address this problem. The objective of this article was to develop a cohesive zone model for rubber to numerically predict crack growth in a rubber component under dynamic tearing. The cohesive zone model for rubber was embedded into the material constitutive equation via a user-defined material subroutine (VUMAT) of ABAQUS. It consisted of three parts: (1) hyperviscoelastic behavior before damage, (2) damage initiation based on the critical strain energy density, and (3) hyperviscoelastic behavior after damage initiation. Crack growth in the tensile strip and pure shear specimens was simulated in ABAQUS Explicit, and good agreement was reported between finite element analysis predictions and test results.

**KEY WORDS:** cohesive zone model, rubber, hyperviscoelastic, finite element analysis

## Introduction

All tires possess microscopic flaws or defects. These flaws gradually coalesce into cracks, and these cracks grow as a result of fatigue or cycling loading in a rotating tire. Occasionally, surface cracks can appear on sidewalls or the base of tread grooves from weathering or ozone cracking. In most cases, crack growth is slow, stable, and sustainable before the treads wear down in the tire. Under some circumstances, however, a crack may grow to a critical length so that further loading results in unstable crack growth and catastrophic failure throughout the tire. Tread separation and sidewall zipper failure are two well-known examples of catastrophic tire failures, which could result in uncontrollable vehicle dynamics and sometimes accidents. Trucks, off-road vehicles, and heavy-equipment vehicles are prone to these types of failures because of an aggressive environment and usage, as well as poor maintenance, such as underinflated tires. Poor materials and manufacturing processes could exacerbate the problem by increasing the number and size of microscopic defects in a tire. New tire technology, such as the introduction or sensors/

Department of Mechanical Engineering, University of Akron, 302 East Buchtel Avenue, Akron, Ohio 44325-3903, USA

<sup>&</sup>lt;sup>2</sup> Corresponding author. Email: bl28@zips.uakron.edu

indicators and a change in materials/manufacturing processes, could also potentially lead to unintentional or unexpected tire response and result in some of these failures. Therefore, it is important to have predictive models and computational tools that can address the growth of cracks in a tire. Having this capability will improve tire engineering and analysis, and it may even alleviate overdesigning them with unsubstantiated high factors of safety.

A cohesive zone model (CZM) for predicting crack propagation in rubber under dynamic loading is developed in this article. This concept is based on the idea of energy release rate, which originated with Griffith [1]. The adaptation of Griffith's energy approach to the tear behavior of rubber was made in 1953 by Rivlin and Thomas [2] and verified experimentally by comparing the behavior of test pieces of very different shapes by Thomas [3]. From the viewpoint of fracture mechanics, a crack will not grow unless the energy release rate exceeds the critical energy release rate or tear energy of the rubber necessary to create a new surface at the crack tip. However, rubber fracture mechanics is distinct from classical fracture mechanics of other engineering materials because it involves hyperviscoelastic material behavior and large deflection or finite strain analysis. In addition to this, rubber's mechanical properties are also affected by aging, temperature, and environmental agents, such as ozone and ultraviolet rays [4].

The energy release rate for crack propagation in an actual tire is a complicated function of the initial crack length and its orientation, tire geometry, rubber material behavior in the tire, and the loading to the tire imparted by the vehicle. There have been attempts to use finite element analysis (FEA) to calculate energy release rates (sometimes called J-Integrals) in tires [5,6]. However, these attempts focused on crack initiation and did not involve the creation of new crack surfaces in the tire. The CZM is a breakthrough in fracture mechanics because it is based on the energy release rate and can describe crack growth or the creation of new surfaces. By introducing the concept of a traction-separation law in a cohesive zone at the crack tip, the crack is assumed to break like two adhesive surfaces. Each material has its own unique traction-separation law depending on micro-mechanisms of failure [7]. The CZM is typically characterized by only two of three parameters: the peak traction  $T_i$ , the maximum displacement  $\delta_f$ , and the energy release rate G, which is the area under the traction-separation curve shown in Fig. 1. In this case, the stress at the crack tip is characterized by the peak traction  $T_i$  so that the CZM avoids the stress singularity problem, which arises with the use of stress intensity factors and J-Integrals.

Although the CZM has been applied in fracture analysis of both brittle and ductile materials, most CZM research requires a predefined crack path in different FEA problems [8–14], including rubber [15]. The approach in this article does not make use of cohesive elements and a predetermined crack path but instead incorporates cohesive zone modeling into the material constitutive

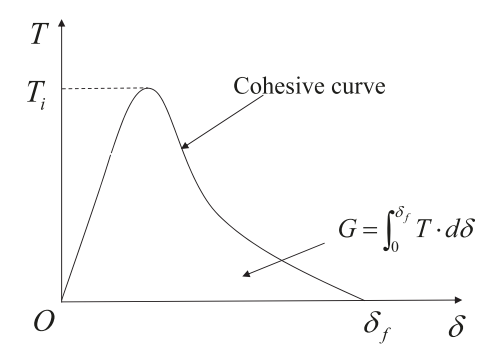


FIG. 1 — Traction-separation law of a cohesive zone model.

behavior of the rubber. To develop the CZM for rubber, results from high-strain-rate material tensile and fracture tests on carbon black-filled natural rubber (NR) are taken from Al-Quraishi and Hoo Fatt [16] and Hoo Fatt et al. [17]. The following section summarizes the above-mentioned experimental results that will be used in this study. A CZM for rubber is then proposed after this. A hyperviscoelastic constitutive equation and a damage initiation criterion are first developed from the high strain rate, uniaxial dumbbell tension test data up to break. Appropriate equivalent traction and displacement then follow from the damage initiation criterion. A unique damage evolution function for rubber is proposed and introduced into the traction-separation response for the rubber. The traction-separation response and the tear energy of the NR are used to determine crack propagation. The CZM model is incorporated in the form of an ABAQUS Explicit user-defined material subroutine (VUMAT) and is used to predict the crack initiation and propagation in the tensile strip and pure shear fracture specimens.

## Charpy Impact Tension and Fracture Test Results

The test data used in this article are taken from references [16] and [17]. In these experiments, a Charpy Tensile Impact apparatus [18] was used to apply tensile loading of rubber specimen at high speeds. The drop height of the Charpy pendulum determined the amount of available potential energy for each test. Once the pendulum was released, it hit a slider bar at the base, thereby transferring potential energy of the hammer to kinetic energy of slider bar. Through various design configurations, the slider bar was connected to ends of grips holding the specimens. Specific details of these can be found in references [16] and [17]. During each test, the deformation and the crack tip position of the specimen were recorded by the FASTCAM-Ultima high-speed camera, and piezoelectric force sensors were used to record the impact tensile force imposed on the specimen.

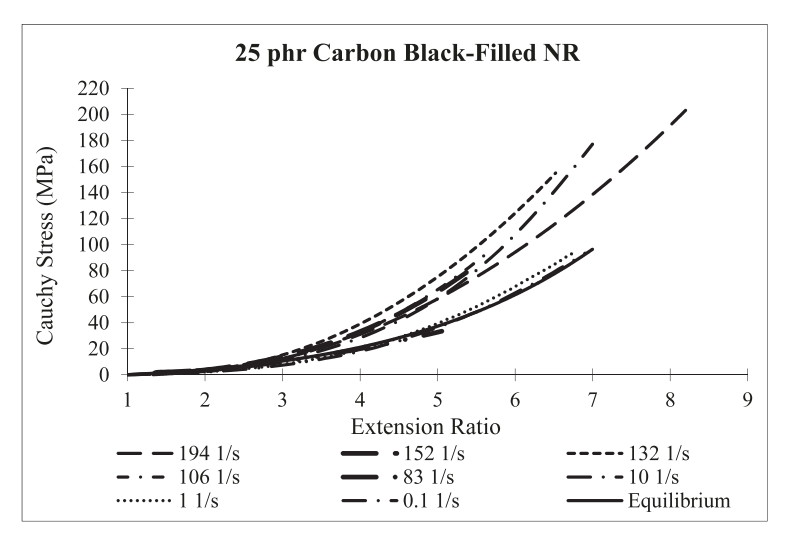


FIG. 2 — Uniaxial tension test results.

Three types of specimens were tested on this Charpy Tensile Impact apparatus: (1) uniaxial tensile dumbbell, (2) tensile strip, and (3) pure shear. The uniaxial tension test results are used to develop the hyperviscoelastic behavior before damage initiation as well as a damage initiation criterion for rubber. The tensile strip and pure shear fracture tests are then used to develop the CZM, including the hyperviscoelastic behavior after damage initiation and tearing. The CZM is used in an ABAQUS Explicit program to simulate tearing of the tensile strip and pure shear specimens. Crack propagation is manifested by element erosion in the FEA.

## Uniaxial Tension Tests

In reference [16], a uniaxial tension test was performed on ASTM D638 half-dumbbell specimens [19]. The experiments were done to break up the material so that the tensile strength and elongation at break could be found, as shown in Fig. 2. In addition to the high-strain-rate tests, material behavior at 0.1, 1, and 10 s<sup>-1</sup> as well as the equilibrium behavior of material were obtained from an MTS servo-hydraulic machine. The equilibrium response was obtained from step relaxation tests on the MTS servo-hydraulic machine. Results from the MTS machine are added to Fig. 2 for comparison. It was noted that the NR exhibited rate-dependent behavior. Unlike most other rubber compounds, stiffness and strength do not increase with the rate of loading because of a lack of relaxation time during the test. NR obtains stiffness and strength from strain-induced crystallization, which is a process that occurs over a finite time. At high

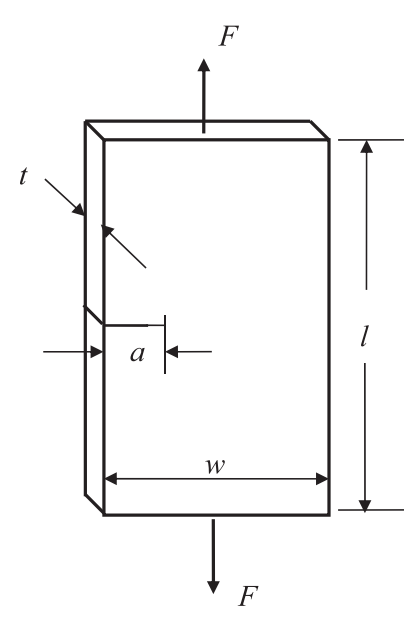


FIG. 3 — Tensile strip specimen.

strain rates or very short loading times, this crystallization process is suppressed so that stiffening and strengthening by it are reduced.

## Tensile Strip Tests

In the tensile strip tests, the specimen was a flat rubber sheet with a notch, as shown in Fig. 3. The dimensions of the specimen were length l = 50.8 mm, width w = 25.4 mm, thickness t = 2 mm, and a notch or precrack length a = 5.08 mm. The tensile loading was evenly imposed on the opposite ends of the specimen. Crack growth occurred from the left end to the right end at the center of the specimen.

The deformation and the corresponding force-displacement relation measured at the grips are shown in Fig. 4 for the test at drop height 76.2 cm. Different stages of deformation and crack growth are marked as a-e, and the corresponding force-displacement curve at these events is given. The specimen experienced severe blunting before fracture onset at 25.6 ms or 50.6 mm of extension. The crack grows from 25.6 ms to 30.7 ms, when the specimen breaks into two parts. Tests at drop heights 50.8 and 101.6 cm were also done, and results from these will be shown in a later section.

## Pure Shear Tests

The pure shear tests were similar to the tensile strip tests. However, the width of the specimen was much longer than its height, as shown in Fig. 5. The

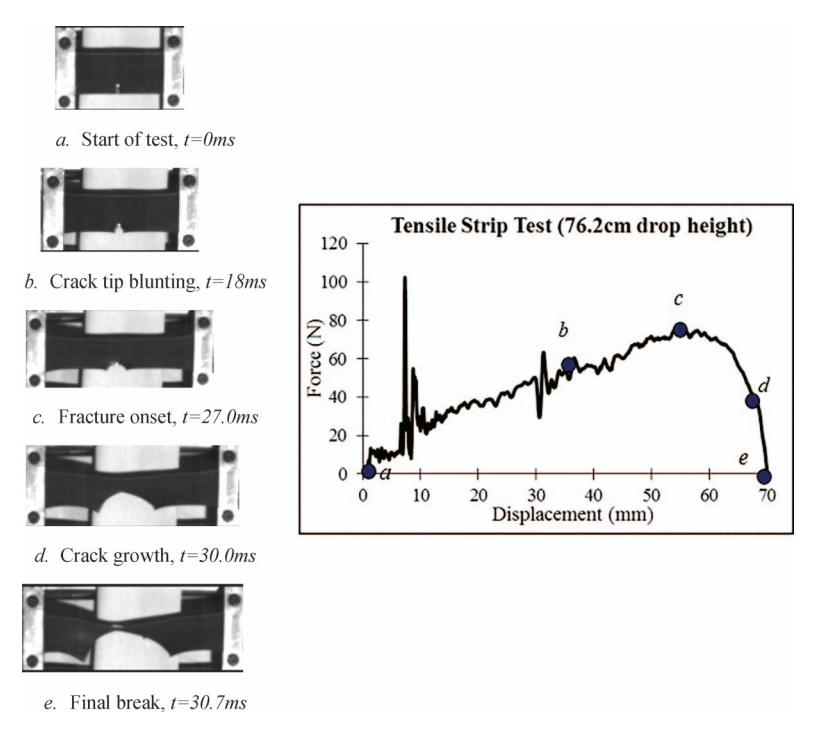


FIG. 4 — Tensile strip test deformation and corresponding force-displacement curve at 76.2-cm drop height.

dimensions of the specimen were height h=19 mm, width w=260 mm, thickness t=1.5 mm, and precrack length a=63.5 mm. During the pure shear tests, tensile loading was imposed on the upper surface of the specimen and the lower surface was fixed. The crack grows from the notch to the right end. The material is under constrained tension because of the high width-to-height ratio. This mode of fracture is often termed *constrained tension* because of this geometry configuration.

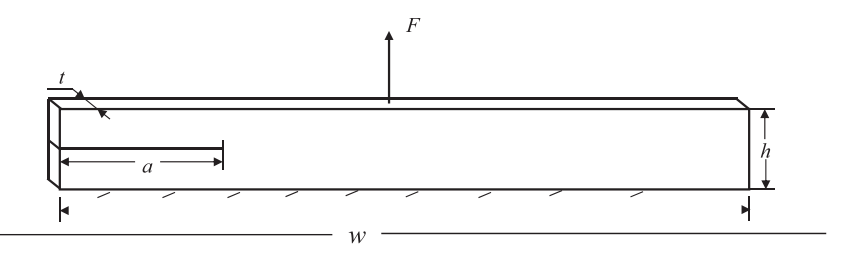


FIG. 5 — Pure shear specimen.

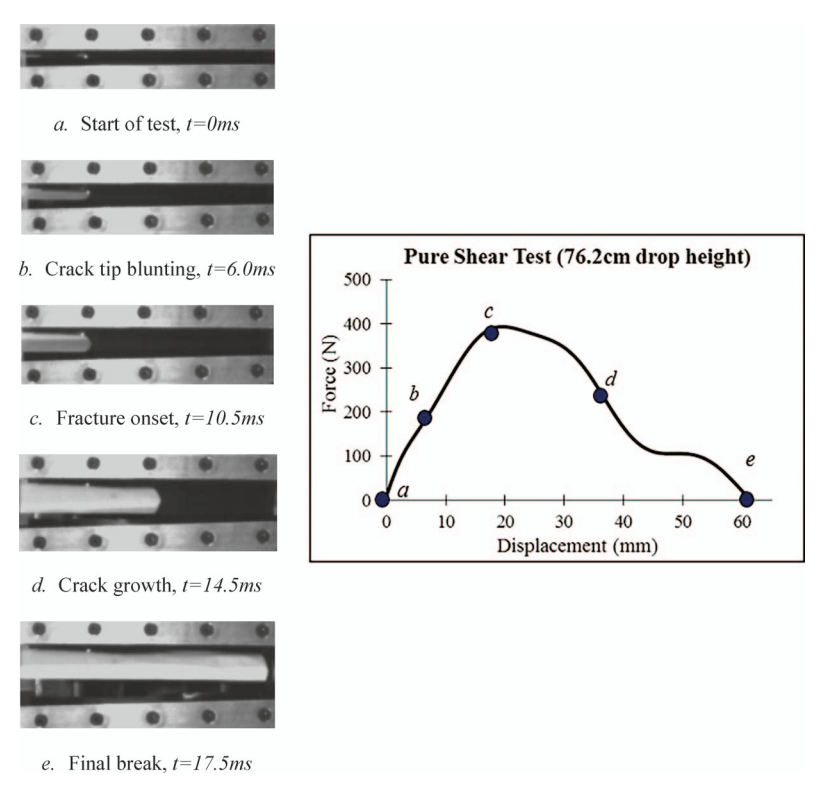


FIG. 6 — Pure shear test deformation and corresponding force-displacement curve at 76.2-cm drop height.

The deformation and the corresponding force-displacement curve measured at the grips are shown in Fig. 6 for the test at 76.2-cm drop height. Similar to the tensile strip, there is blunting at the crack tip before the onset of fracture at 10.5 ms or 18 mm. Crack growth in this specimen is much longer than the tensile strip. The load drop that is associated with tearing occurs over half of the total load-drop curve so that crack propagation in this specimen is very evident. Tests at drop heights of 50.8 and 101.6 cm were also performed, and results from these will be given in a later section.

## **Development of CZM for Rubber**

During crack growth in a ductile material—like rubber, there is an apparent cohesive zone ahead of the crack tip as shown in Fig. 7a. From the viewpoint of a CZM, material behavior in the cohesive zone can be characterized by an equivalent traction-separation law, as shown in Fig. 7b. The stress at the crack tip is denoted by an equivalent traction *T*, and the displacement between the two

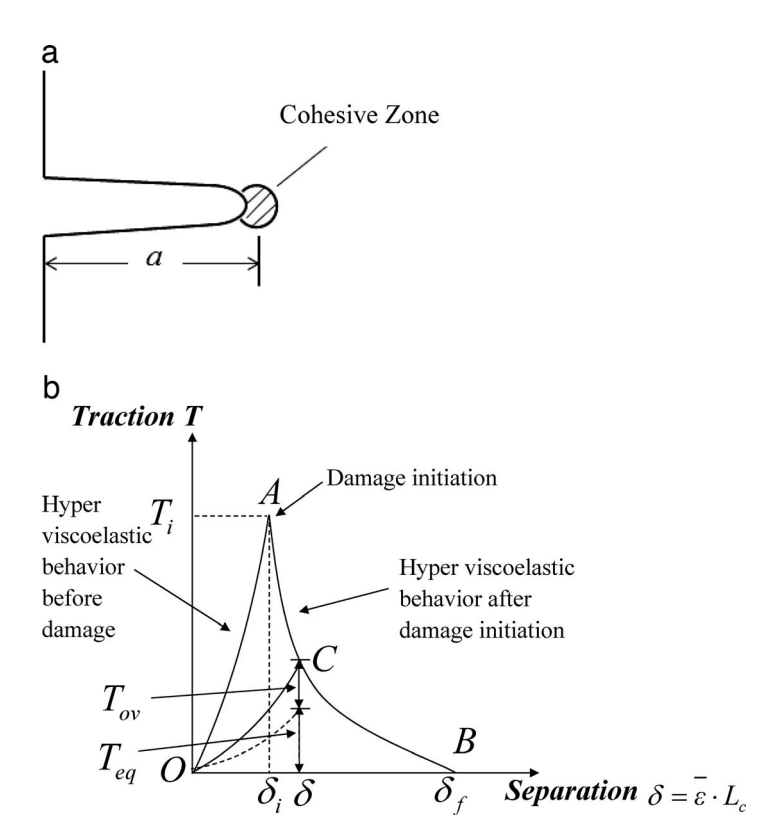


FIG. 7 — Growth of a crack in rubber: (a) cohesive zone and (b) equivalent traction-separation law.

surfaces ahead of the crack tip is denoted by an equivalent separation  $\delta$ , which is given by

$$\delta = \bar{\epsilon} \cdot L_c \tag{1}$$

where  $\bar{\epsilon}$  is the equivalent strain and  $L_c$  is the characteristic length associated with the mesh in FEA. Specific details of how to obtain the equivalent strain and traction at the crack tip will be given later.

The CZM that is proposed for rubber consists of three events based on the equivalent traction-separation law: (1) hyperviscoelastic behavior before damage OA, (2) damage initiation at A, and (3) hyperviscoelastic behavior after damage initiation AB. Note that in most existing CZMs, behavior before damage OA is ignored because it is used with cohesive surface or interface elements and not actual material response.

OA, the hyperviscoelastic behavior before damage is developed from a rheological model involving an equilibrium spring, is in parallel with a Maxwell

element. The high-strain-rate, uniaxial tension test data up to break is used to develop this hyperviscoelastic behavior.

At Point A, the critical strain energy density is selected as the damage initiation criterion for the rubber material. A strain rate–dependent function is used to describe the variation of critical strain energy density in a different strain rate. In the equivalent traction-separation curve  $T_i$  and  $\delta_i$  are, respectively, the traction and displacement when the damage initiation is reached.

In AB, the hyperviscoelastic behavior after damage initiation is characterized by the following exponential function:

$$T = T_i \left\{ 1 - \left[ \frac{1 - e^{\frac{-m(\delta - \delta_i)}{(\delta_f - \delta_i)}}}{1 - e^{-m}} \right] \right\}$$
 (2)

where m is a parameter to control the rate of degradation and  $\delta_f$  is the final displacement. The equivalent traction T is given by

$$T = T_{eq} + T_{ov} \tag{3}$$

where  $T_{eq}$  is the equivalent traction due to equilibrium spring and  $T_{ov}$  is the equivalent traction due to intermediate spring. Hence, the equivalent traction is hyperviscoelastic. The tear energy of the rubber G is the value equal to the area under OAB:

$$G = \int_0^{\delta_f} T d\delta \tag{4}$$

Once damage has initiated, the material properties are degraded. It is important to distinguish the terms damage and degradation in this context with the so-called Mullins effect or stress softening in the hysteresis of filled rubbers undergoing cyclic loading [20]. Here the terms damage and degradation relate to the local cavitation or thinning of a rubber sheet as it breaks apart. Figure 8a and b illustrate the loading-unloading behavior of rubber in the undamaged and damaged states. Between OA, the rubber has hyperviscoelastic behavior with undamaged properties, as shown in Fig. 8a. Between AC, the rubber has hyperviscoelastic behavior with damaged properties, as shown in Fig. 8b. Loading and unloading in these deformation phases produce hysteresis. Unloading between AC can occur if the available energy is not enough to create new surfaces. The following section describes the material behavior before damage, a damage initiation criterion, and material behavior after damage initiation based on the above CZM for rubber.

## Hyperviscoelastic Behavior before Damage

The hyperviscoelastic behavior of the NR is derived from the rheological model of an equilibrium spring in parallel with a Maxwell element, as shown in

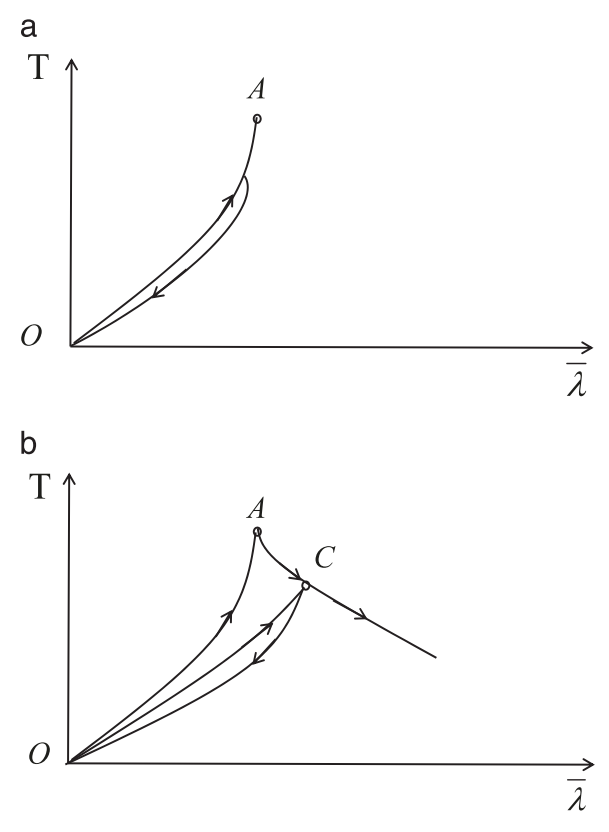
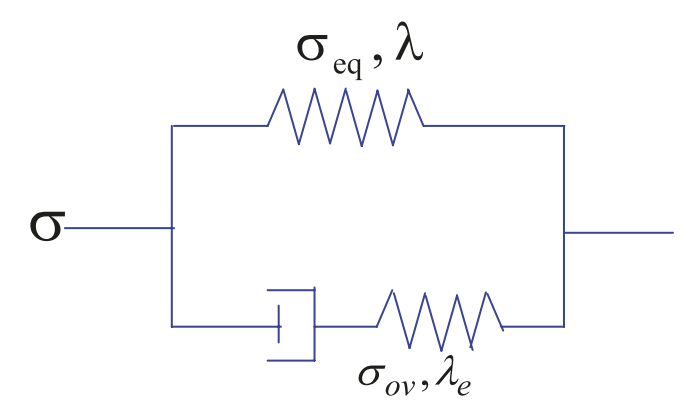


FIG. 8 — Loading-unloading behaviors in (a) undamaged state and (b) damaged state.



 $FIG.\ 9-{\it Rheological\ model\ for\ a\ hyperviscoelastic\ material}.$ 

Fig. 9. The Maxwell element has a viscous damper in series with an intermediate spring. Thus, the total stress at any time is given by

$$\sigma = \sigma_{ea} + \sigma_{ov} \tag{5}$$

where  $\sigma$  symbolizes the total Cauchy stress of this model. The  $\sigma_{eq}$  and  $\sigma_{ov}$  denotes the stress caused by the equilibrium spring and intermediate spring, respectively. Both springs in this model are hyperelastic, and resistance of the viscous damper is controlled by strain rate.

The viscous damper allows the force in the intermediate spring to vary at different strain rates. If the strain rate is very low or approaches zero, the total deformation of this rheological model is governed only by the equilibrium spring since no force passes through the intermediate spring of the Maxwell element. In this case, the total stress  $\sigma$  is equal to the equilibrium stress  $\sigma_{eq}$ . When the strain rate is very high, the viscous damper does not have time to deform, and the intermediate spring deforms by the same amount as the equilibrium spring. In this case, the overstress and total stress are at an upper limiting value. In between very slow and fast strain rates, the intermediate spring deformation is lower than the equilibrium spring. This feature allows rate-dependent behavior to be modeled.

In a three-dimensional context, the equilibrium and intermediate springs are expressed as incompressible hyperelastic material:

$$\sigma_{eq} = -p_{eq}I + 2\left(\frac{\partial U_{eq}}{\partial I_1} + I_B \frac{\partial U_{eq}}{\partial I_2}\right)B - 2\frac{\partial U_{eq}}{\partial I_2}BB \tag{6}$$

and

$$\sigma_{ov} = -p_{ov}I + 2\left(\frac{\partial U_{ov}}{\partial I_{1e}} + I_{1e}\frac{\partial U_{ov}}{\partial I_{2e}}\right)B_e - 2\frac{\partial U_{ov}}{\partial I_{2e}}B_eB_e \tag{7}$$

where  $p_{eq}$  and  $p_{ov}$  are undetermined pressures,  $I_1$  and  $I_2$  denote first and second invariants of the left Cauchy Green deformation tensor B in the equilibrium spring,  $I_{1e}$  and  $I_{2e}$  denote first and second invariants of the left Cauchy Green deformation tensor in the intermediate spring  $B_e$ , and  $U_{eq}$  and  $U_{ov}$  are strain energy potential functions given in terms of the above-mentioned invariants of the left Cauchy Green deformation tensors.

The key to relating viscosity to the overstress lies in a compatibility relation first derived by Huber and Tsakmakis [21]:

$$\dot{B_e} = LB_e + B_e L^{\mathrm{T}} - 2F_e D_v F_e^{\mathrm{T}} \tag{8}$$

where L is the velocity gradient tensor and  $D_{\nu}$  is the rate of deformation tensor of the viscous damper. They argued that to guarantee the dissipation rate is always positive

$$F_e D_v F_e^T = \frac{1}{\eta} B_e \sigma_{ov}^D, \eta > 0 \tag{9}$$

where  $\eta$  is a viscosity coefficient and  $\sigma_{ov}^D$  is the deviatoric component of the overstress. Substituting Eq. (9) into Eq. (8) gives an expression for the overstress in terms of the

$$\dot{B_e} = LB_e + B_e L^T - \frac{2}{\eta} B_e \sigma_{ov}^D \tag{10}$$

The above equation relates the overstress to deformation rates in both equilibrium and intermediate springs. In reference [21],  $\eta$  was assumed to be constant, but in this article,  $\eta$  is taken to be a nonlinear function of  $I_1$  and  $I_{1e}$ . By making the viscosity a function of the first invariants of both of these left Cauchy Green deformation tensors, the overstress becomes dependent on deformation as well as rate of deformation.

The above expressions were reduced to the uniaxial stress case in order to obtain hyperelastic constants for the springs and a viscosity function for the damper. A Yeoh (third-order reduced polynomial) function [22] was found to best describe the hyperelastic equilibrium and intermediate springs, which were assumed to have the same hyperelastic coefficients for simplicity:

$$\sigma_{eq} = 2\left[C_{10} + 2C_{20}(I_1 - 3) + 3C_{30}(I_1 - 3)^2\right] \left(\lambda^2 - \frac{1}{\lambda}\right), \ I_1 = \lambda^2 + \frac{2}{\lambda} \quad (11)$$

and

$$\sigma_{ov} = 2\left[C_{10} + 2C_{20}(I_{1e} - 3) + 3C_{30}(I_{1e} - 3)^2\right] \left(\lambda_e^2 - \frac{1}{\lambda_e}\right), \ I_{1e} = \lambda_e^2 + \frac{2}{\lambda_e}$$
(12)

The hyperelastic coefficients,  $C_{10}$ ,  $C_{20}$ , and  $C_{30}$ , were found by fitting the uniaxial test data from a step relaxation tests for the equilibrium response. For the 25 phr carbon black-filled NR:  $C_{10} = 0.2515$  MPa,  $C_{20} = 0.0057$  MPa, and  $C_{30} = 6.303$ E-06 MPa. Once these coefficients were found, a viscosity function was derived from the high strain rate tests as follows:

$$\eta = a(I_1 + b)^c + d(I_{1e} + e)^f + g(I_1 + h)^i (I_{1e} + j)^k + l$$
(13)

where parameters a-l are listed in Table 1. Figure 10 is a plot showing the viscosity in  $I_1$ - $I_{1e}$  space.

Uniaxial stress-strain behavior at various strain rates was predicted with the above hyperelastic and viscoelastic properties. The predicted hyperviscoelastic behavior before damage initiation is compared in tensile tests results in Fig. 11a and b, and relatively good agreement is reported.

| Parameter | $I_1 < 9.67$ | $I_1 > 9.67$ |
|-----------|--------------|--------------|
| a (MPa.s) | 0.409455     | 154.7404     |
| b         | -1.29823     | -1.9         |
| c         | -0.61508     | 0.051 397    |
| d (MPa.s) | -1.10048     | 72.244 54    |
| е         | 109.5941     | -1.88472     |
| f         | -0.21383     | 0.296 595    |
| g (MPa.s) | 0.091817     | -22.6715     |
| h         | 209.7806     | 42.7413      |
| i         | 0.255 25     | 0.795 111    |
| j         | -1.9         | -0.12447     |
| k         | 0.499 024    | -0.4608      |
| l (MPa.s) | -0.26139     | 78.941 04    |

TABLE 1 — Parameters for NR25 viscosity function.

## Damage Initiation Criterion

The damage initiation criterion for NR is defined as the critical strain energy density  $U_{crit}$ , which is the total strain energy density stored in the equilibrium and intermediate spring up to break in a uniaxial tensile test. At point A, the strain energy density U is given by

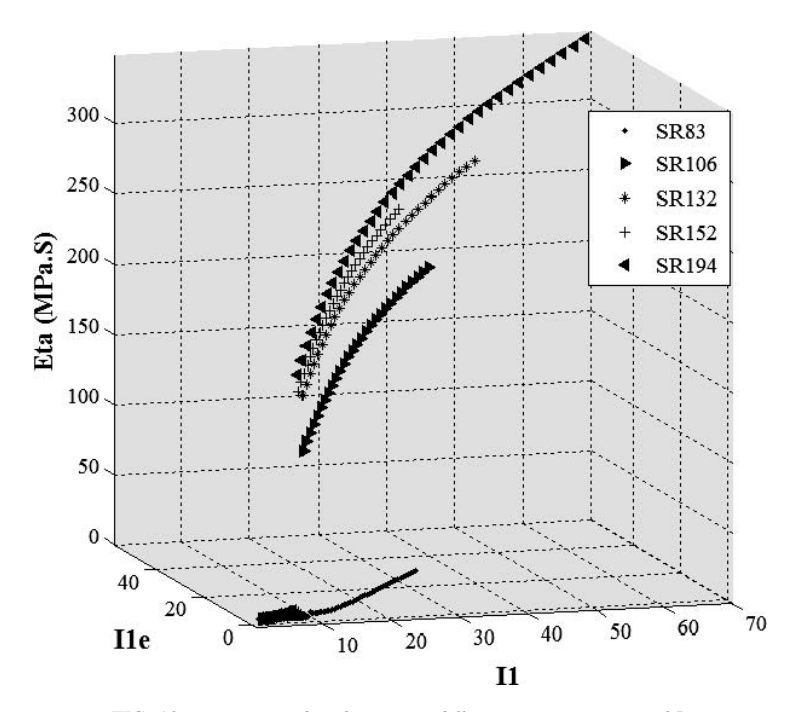
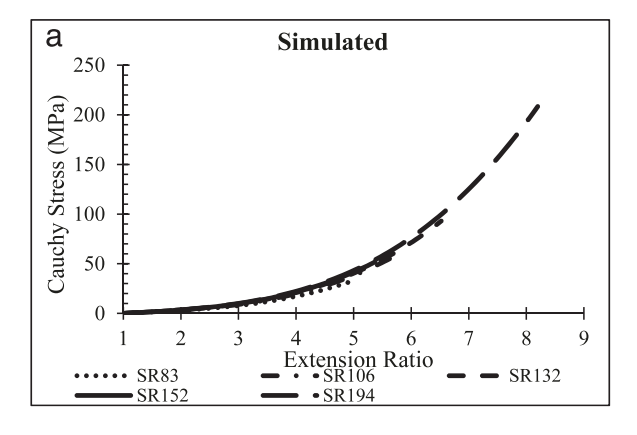


FIG. 10 — Viscosity distributions at different strain rate in NR25.



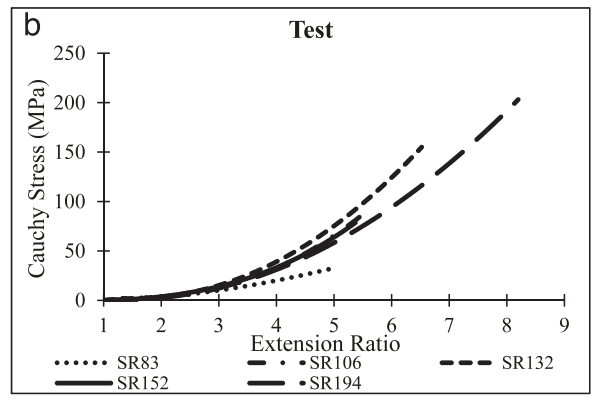


FIG. 11 — Rate-dependent material response: (a) simulations and (b) tests.

$$U = U_{eq} + U_{ov} \tag{14}$$

where

$$U_{eq} = C_{10}(I_1 - 3) + C_{20}(I_1 - 3)^2 + C_{30}(I_1 - 3)^3$$
 (15)

and

$$U_{ov} = C_{10}(I_{1e} - 3) + C_{20}(I_{1e} - 3)^{2} + C_{30}(I_{1e} - 3)^{3}$$
(16)

Thus, the damage initiation criterion for NR is given by

$$U \ge U_{crit}$$
 (17)

The critical strain energy density is rate dependent. The tensile strength and elongation at break depended on strain rate in the tensile tests. To model this rate dependency, the following function was chosen for  $U_{crit}$ :

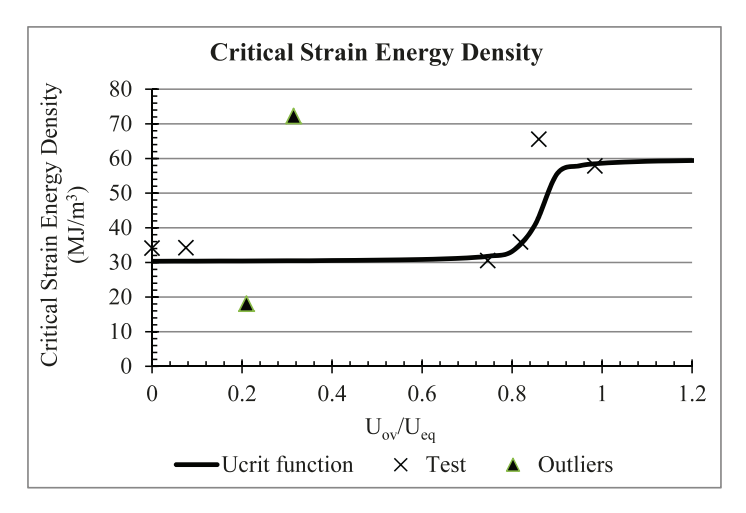


FIG. 12 — Damage initiation function based on Ucrit.

$$U_{crit} = c_1 \cdot \arctan\left(c_2\left(\frac{U_{ov}}{U_{eq}}\right) + c_3\right) + c_4 \tag{18}$$

where  $\frac{U_{ov}}{U_{eq}}$  is the ratio of elastic strain energies in the intermediate and equilibrium springs at break,  $c_1 = 9\,500$  kJ/m<sup>3</sup>,  $c_2 = 50.0$ ,  $c_3 = -43.0$ , and  $c_4 = 40\,500$  kJ/m<sup>3</sup>. A plot of this function and the calculated tensile test results is given in Fig. 12. The tests at 83 s<sup>-1</sup> and 194 s<sup>-1</sup> were considered outliers.

## Hyperviscoelastic Behavior after Damage Initiation

Recall from Fig. 7b that behavior after damage initiation is specified by the exponential damage evolution function. The equivalent traction and separation for this evolution function are defined in this section.

Damage evolution is a series of damage initiation events. As stated in the previous section, damage initiates at a critical value of the strain energy density. Let  $\overline{I_1}$  and  $\overline{I_{1e}}$  be the values of the first invariant of the left Cauchy Green deformation tensors when the sum of  $U_{eq}$  and  $U_{ov}$  reaches  $U_{crit}$ . These define equivalent stretch ratios,  $\bar{\lambda}$  and  $\bar{\lambda_e}$ , for an incompressible material since

$$\overline{I_1} = \overline{\lambda}^2 + \frac{2}{\lambda} \tag{19}$$

and

$$\overline{I_{1e}} = \overline{\lambda_e}^2 + \frac{2}{\lambda_e} \tag{20}$$

The equivalent stretch ratio  $\bar{\lambda}$  due to equilibrium spring is determined by the largest root of the following cubic equation:

$$\bar{\lambda}^3 - \bar{I}_1 \bar{\lambda} + 2 = 0 \tag{21}$$

Therefore, the equivalent traction due to the equilibrium spring  $T_{eq}$  is given by

$$T_{eq} = 2\left(\bar{\lambda}^2 - \frac{1}{\bar{\lambda}}\right)C_{10d}\left[1 + 2a_1\left(\bar{\lambda}^2 + \frac{2}{\bar{\lambda}} - 3\right) + 3a_2\left(\bar{\lambda}^2 + \frac{2}{\bar{\lambda}} - 3\right)^2\right]$$
(22)

where  $C_{10d}$ ,  $C_{20d}$ , and  $C_{30d}$  are the damaged parameters in Yeoh function and  $a_1 = \frac{C_{20}}{C_{10}}$  and  $a_2 = \frac{C_{30}}{C_{10}}$  are the ratios measured when damage initiated. It is assumed that these ratios remain constant during damage evolution. Furthermore, the equivalent strain is  $\bar{\epsilon} = \bar{\lambda} - 1$ , and the equivalent displacement is  $\delta = \bar{\epsilon} \cdot L_c$ .

Similarly, the equivalent stretch ratio  $\bar{\lambda}_e$  due to intermediate spring is determined by the largest root of

$$\bar{\lambda}_e^3 - I_{1e}\bar{\lambda}_e + 2 = 0 \tag{23}$$

and, the equivalent traction due to the intermediate spring  $T_{ov}$  is given by

$$T_{ov} = 2\left(\bar{\lambda}_{e}^{2} - \frac{1}{\bar{\lambda}_{e}}\right)C_{10d}\left[1 + 2a_{1}\left(\bar{\lambda}_{e}^{2} + \frac{2}{\bar{\lambda}_{e}} - 3\right) + 3a_{2}\left(\bar{\lambda}_{e}^{2} + \frac{2}{\bar{\lambda}_{e}} - 3\right)^{2}\right]$$
(24)

The equivalent traction is now specified simultaneously by Eq. (2) and the sum of Eqs. (22) and (24). Setting these expressions equal to each other gives

$$C_{10d} = \frac{T_i \left\{ 1 - \frac{1 - e^{\frac{-m(\delta - \delta_i)}{\delta_j - \delta_i}}}{1 - e^{-m}} \right\}}{2\left(\bar{\lambda}^2 - \frac{1}{\bar{\lambda}}\right) \left[ 1 + 2a_1\left(\bar{\lambda}^2 + \frac{2}{\bar{\lambda}} - 3\right) + 3a_2\left(\bar{\lambda}^2 + \frac{2}{\bar{\lambda}} - 3\right)^2 \right]} + 2\left(\bar{\lambda}_e^2 - \frac{1}{\bar{\lambda}_e}\right) \left[ 1 + 2a_1\left(\bar{\lambda}_e^2 + \frac{2}{\bar{\lambda}_e} - 3\right) + 3a_2\left(\bar{\lambda}_e^2 + \frac{2}{\bar{\lambda}_e} - 3\right)^2 \right]}$$
(25)

This function decreases as  $\delta$  or  $\bar{\lambda}$  increases. The above expression for  $C_{10d}$  allows one to completely determine all Yeoh hyperelastic coefficients after damage because  $C_{20d}=a_1C_{10d}$  and and  $C_{30d}=a_2C_{10d}$ . These hyperelastic coefficients approach zero when  $\delta=\delta_f$ .

To calculate  $\delta_f$ , first consider the area under OA in Fig. 7b and denote it as

$$G_1 = \int_0^{\delta_i} Td\delta \tag{26}$$

Numerically, this is done by calculating the internal energy per unit volume and

| ABAQUS solver | Dynamic, explicit version 6.12   |  |
|---------------|--|--|
| Element       | $l \times b \times h = 0.125 \text{ mm} \times 0.125 \text{ mm} \times 0.125 \text{ mm}$ ; type = C3D8 |  |
| Step time     | 0.1 s  |  |
| Loading type  | Displacement control, ramp at 13.25 mm/s (strain rate is $106 \text{ s}^{-1}$ )                        |  |

TABLE 2 — ABAQUS single-element model.

multiplying it by  $L_c$ . The remaining energy release rate includes the area under curve AB in Fig. 7b and is given by

$$G_2 = \int_{\delta_i}^{\delta_f} T_i \left\{ 1 - \left[ \frac{1 - e^{\frac{-m(\delta - \delta_i)}{(\delta_f - \delta_i)}}}{1 - e^{-m}} \right] \right\} d\delta = \frac{T_i(\delta_f - \delta_i)[1 - e^{-m}(m+1)]}{m(1 - e^{-m})}$$
(27)

Using  $G_2 = G - G_1$  gives the final equivalent displacement for total damage as

$$\delta_f = \delta_i + \frac{(G - G_1)m(1 - e^{-m})}{[1 - e^{-m}(m+1)]T_i}$$
(28)

The viscosity function after damage initiation also changes with  $C_{10d}$ . A simple function for the viscosity after damage initiation is assumed as

$$\eta_d = \frac{C_{10d}}{C_{10}} \eta \tag{29}$$

where  $\eta$  is the undamaged viscosity function in Eq. (13).

## **FEA Results**

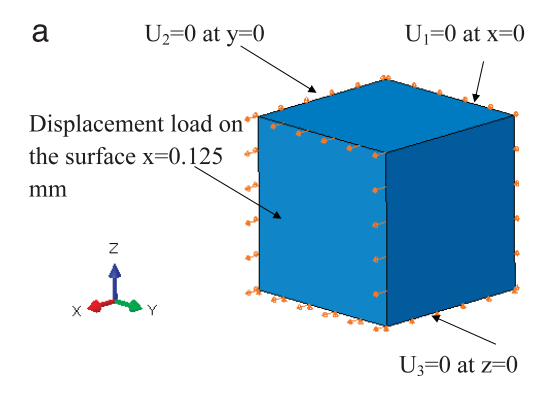
## FEA Implementation

The CZM developed for rubber and discussed above is incorporated in an ABAQUS VUMAT. The VUMAT was first used in a single element under uniaxial stress. The tension test at  $106 \, {\rm s}^{-1}$  strain rate was simulated specifically. Details of the ABAQUS single-element model are given in Table 2, and input material properties are given in Table 3.

Figure 13a shows the element and the boundary conditions applied to it in order to keep it in uniaxial loading condition. The Cauchy extension ratio responses of the single element with a different rate of degradation parameters m are shown in Fig. 13b for comparison. The single-element FEA shows that the load gradually drops after damage initiation. This is different from the sudden load drop in an ideally brittle material. The load drop speed and the final extension of the element depend on m. When  $m \le 0.1$ , an almost linear load drop and a final extension ratio of about 8 is expected. When  $m \ge 5$ , the load drop is steeper at first and ends more gradually, like an exponential

TABLE 3 — Material properties for FEA input.

| 1083.35 kg/m <sup>3</sup>                       |
|---|
| $C_{10} = 0.2515 \text{ MPa}$                   |
| $C_{20} = 0.00568 \text{ MPa}$                  |
| $C_{30} = 6.3029 \text{E} \cdot 06 \text{ MPa}$ |
| $K_1 = 0.251456 \text{ GPa}$                    |
| $K_2 = 0.002838 \text{ GP}$                     |
| $K_{3} = 2.10e-6 \text{ GPa}$                   |
| Eq. (13)  |
| Eq. (18)  |
| 10 900 J/m <sup>2</sup>                         |
| 0.1, 1, 2, 5                                    |
|   |



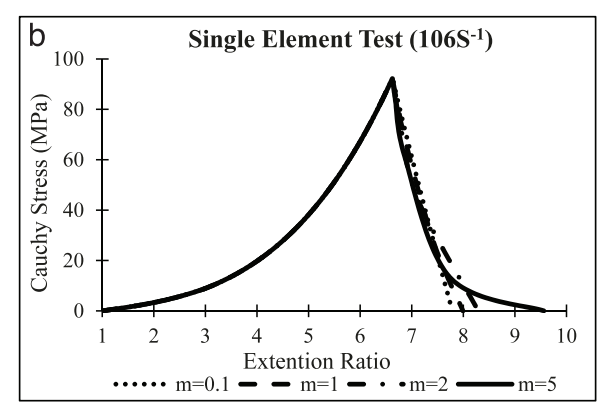


FIG. 13 — Uniaxial tension in a single finite element (a) FEA model and (b) Cauchy stress versus extension ratio with various m.

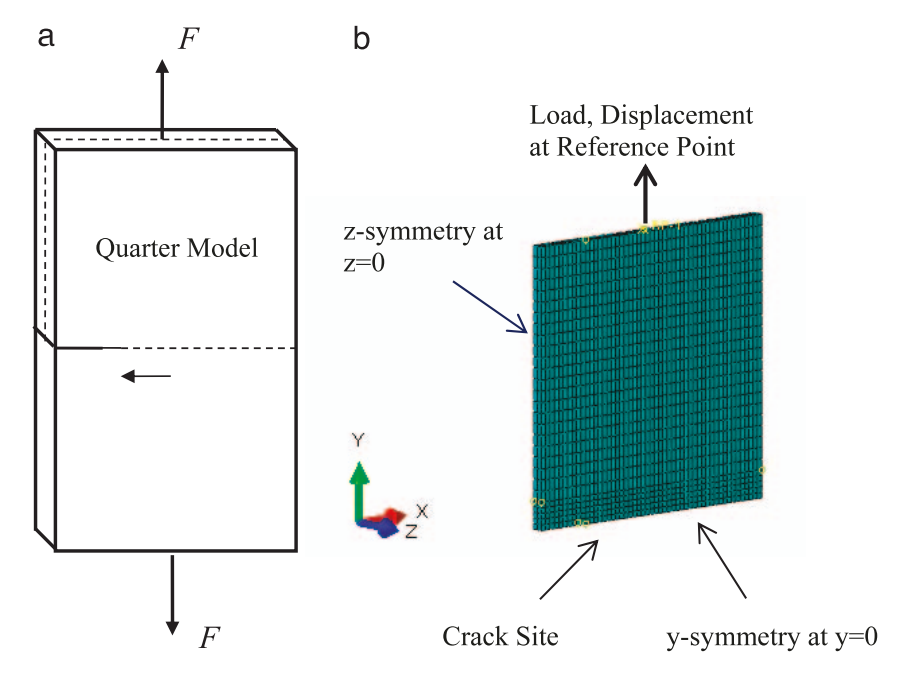


FIG. 14 — FEA model of tensile strip specimen: (a) full specimen and (b) quarter model.

decay, but the final extension ratio becomes large (>9). Such a large extension ratio would not be practical because of element overdistortion. Therefore, there is a small range of useful values for m, and it is assumed that  $0.1 \le m \le 5$ .

In a meshed part, *m* should theoretically control the rate of crack growth because it determines the final deformation at which an element is eroded. The element is eroded quickly when the final deformation is small, and it is eroded slowly when the final deformation is large. However, the size of the element in a meshed part will also affect how fast crack growth is simulated in FEA. Erosion with smaller elements is slower than with larger elements. These are tradeoffs that one has to make in the FEA.

## Tensile Strip Tests

A quarter model of the tensile strip specimen is made to simulate the tensile strip tearing tests because the load is evenly imposed on the specimen opposite ends. The full specimen and quarter model are shown in Fig. 14a and b. The dashed lines in Fig. 14a indicate the quarter of the full strip used in the FEA. According to Fig. 14b, there are symmetry boundary conditions with respect to y and z directions, and the displacement loading is placed at a

| ABAQUS solver     | Dynamic, Explicit Version 6.12             |  |
|-------------------|--|--|
| Geometry          | 1/2 = 25.4  mm (half length)               |  |
| -                 | w = 25.4  mm (width)                       |  |
|                   | t/2 = 1.04 mm (half thickness)             |  |
| Elements          | C3D8, 8-node linear full-integration brick |  |
|                   | No. of elements $= 8058$                   |  |
| Loading type      | 76.2-cm drop height, tensile strip         |  |
| Crack parameter m | m = 5                                      |  |
| Step time         | 35 ms                                      |  |
| Run time          | ∼42 h (4 CPU)                              |  |

TABLE 4 — FEA details of quarter model of tensile strip specimen.

reference point on the top of the surface. Forces are also obtained from this reference point.

Details of the FEA of the tensile strip are given in Table 4. A crack growth parameter of m=5 was chosen to best simulate crack growth. The elements near the crack tip and in the crack path need to be very small order to accurately determine strain energy density and other crack tip parameters. As a result of this, the program run time is about 42 hours with a 4-CPU multicore computer workstation.

The specimen during deformation and tearing from the FEA is compared with the images taken from the tests in Fig. 15. There is very good agreement between the two responses. Blunting at the crack tip and tearing of the tensile strip specimen were successfully simulated in the FEA. A close-up view of the crack tip is shown in Fig. 16. The force and crack growth history from the FEA is compared with that of the test in Fig. 17a-b, and good agreement is also obtained. Both the peak load at the onset of tearing and the load drop during tearing are correctly determined. The initiation and final time of crack growth are also in very good agreement with the test. Two other tensile strip experiments at drop heights of 50.8 and 101.6 cm were also simulated. Good agreement was also found for these, as shown in Fig. 17c-f.

#### Pure Shear Tests

Although the bottom grip of the pure shear specimen was fixed, preliminary FEA shows that a quarter model is still applicable. The full specimen and quarter model of it are shown in Fig. 18a and b. The dashed lines in Fig. 18a indicate the quarter of the specimen used in FEA. According to the Fig. 18b, there are symmetry boundary conditions with respect to *y* and *z* directions. Displacement loading is placed at the reference point on the top of the surface. The grip force is also taken at this reference point. Full details of the FEA of the

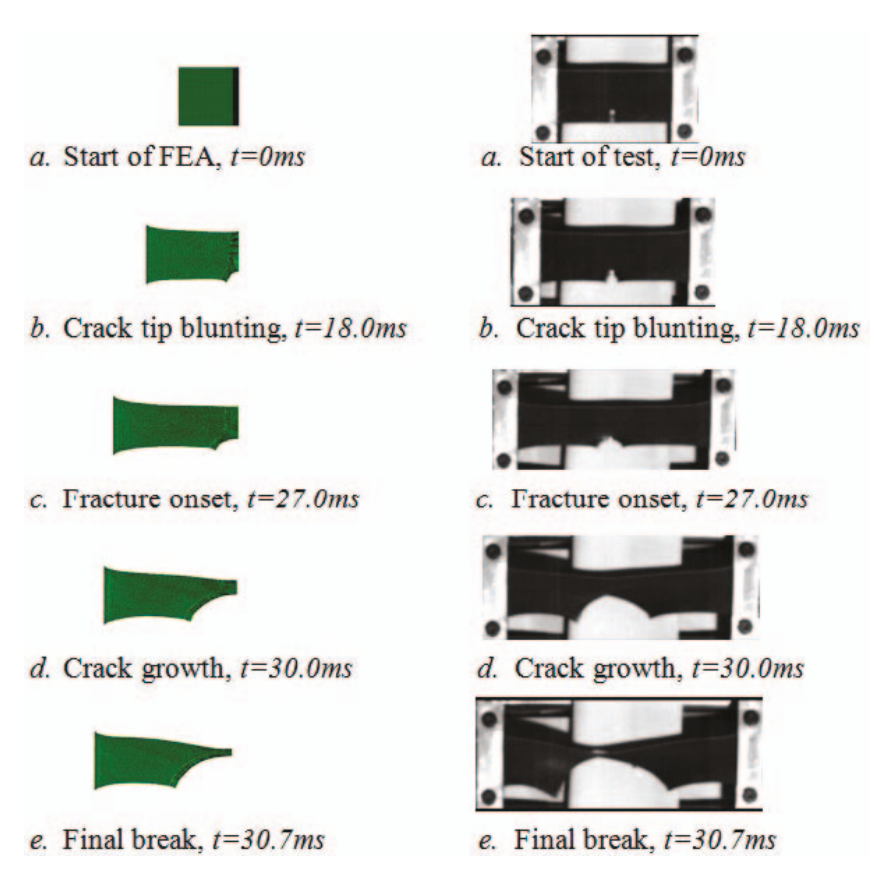


FIG. 15 — Side-by-side comparison of tensile strip tearing in FEA and test for 76.2-cm drop height.

pure shear specimen are given in Table 5. It was not possible to use a smaller mesh in this specimen without excessively increasing the computer run time. To compensate for the larger elements, the critical strain energy density function was reduced by a factor of 1/11.

The specimen deformation from the FEA is compared with the test results in Fig. 19. As with the tensile strip, there is very good agreement between the FEA predicted response and the test images of the pure shear specimen. Blunting at the crack tip and tearing of the specimen were also successfully simulated in the pure shear specimen in the FEA. A close-up view of the crack tip is shown in Fig. 20.

The force and crack growth history from the FEA is compared with that of the test in Fig. 21a-b, and relatively good agreement is also obtained. The

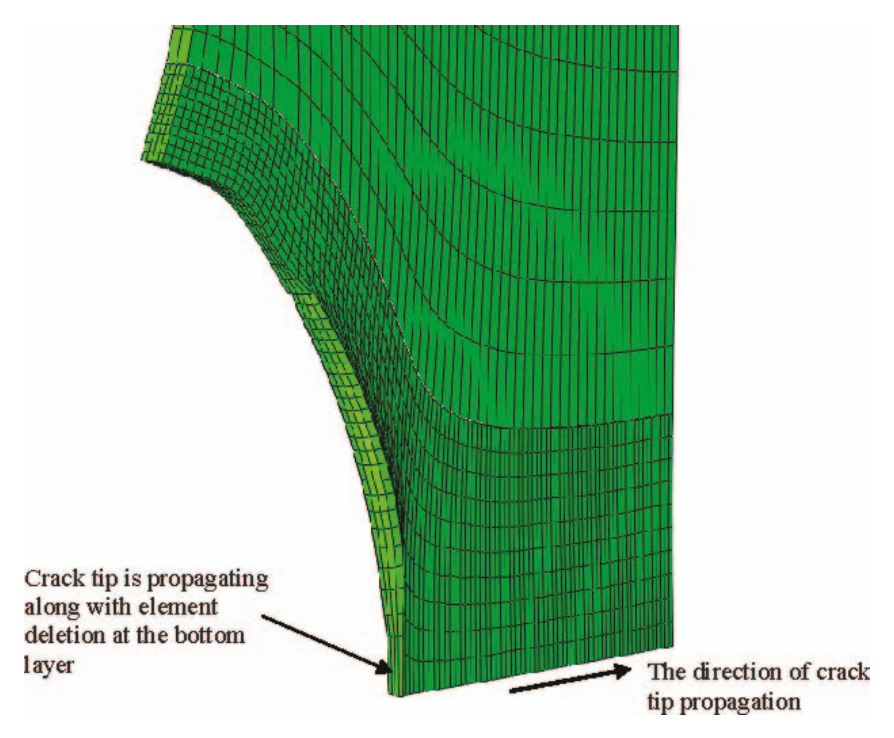


FIG. 16 — Close-up view of crack tip of tensile strip specimen during test at 76.2-cm drop height.

peak load at the beginning of tearing was determined by the FEA very well, and the subsequent load drop during tearing was slightly faster in the FEA than in the test. The corresponding crack speed is faster in the FEA than in the test. Two other pure shear experiments at drop heights of 50.8 and 101.6 cm were also simulated. The peak load was predicted correctly for a drop height of 50.8 cm in Fig. 21c, but FEA again predicted faster tearing than what was reported in the experiment (Fig. 21d). However, very good agreement in both peak load and crack speed was obtained for the 101.6-cm drop height in Fig. 21e–f.

Even though the FEA results with coarser mesh for the wider pure shear specimens were not as accurate as for the tensile strips, they were still able to capture crack initiation and growth in these specimens relatively well. It should be emphasized that m = 5 afforded the lowest crack speed in the FEA, and it was not possible to simulate a slower crack speed in the FEA with this mesh. A finer mesh could improve crack speed accuracy, but this comes at a cost of increased program run time.

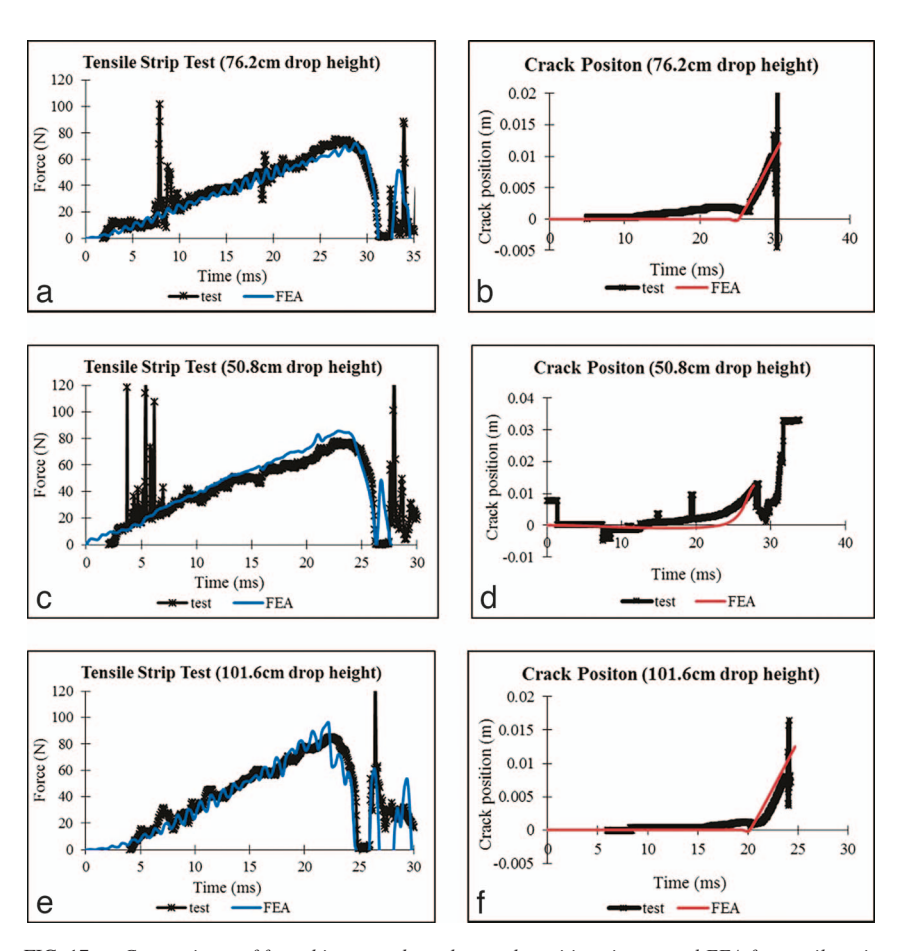


FIG. 17 — Comparisons of force history and crack growth positions in test and FEA for tensile strip experiments at drop heights (a–b) 76.2 cm, (c–d) 50.8 cm, and (e–f) 101.6 cm.

## Conclusions

A CZM for rubber was developed to numerically predict crack growth in a rubber component under dynamic loading. This CZM consisted of three parts: (1) hyperviscoelastic behavior before damage, (2) damage initiation based on the critical strain energy density, and (3) hyperviscoelastic behavior after damage initiation. The CZM for rubber was embedded into the material constitutive equation via a user-defined material subroutine (VUMAT) of ABAQUS Explicit. This allowed crack growth to proceed by element erosion in the FEA programs without predefining a crack path.

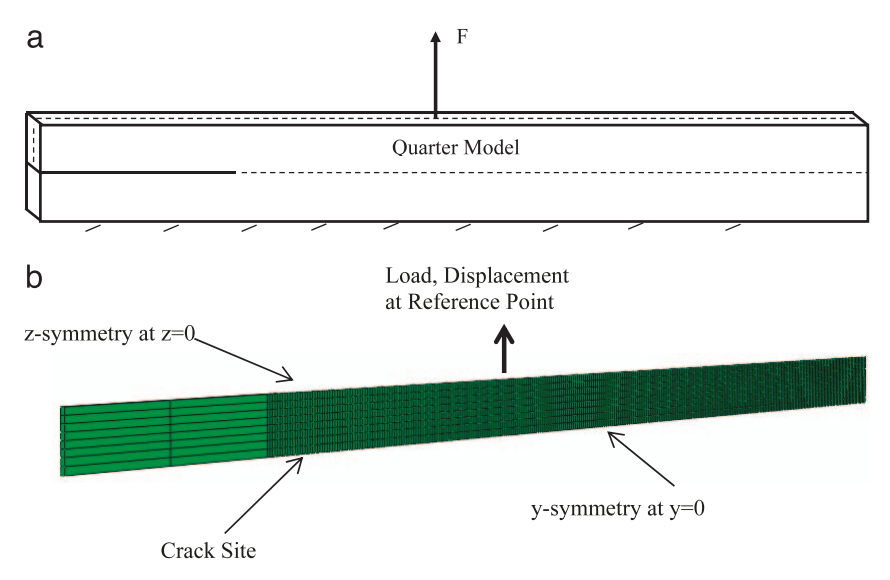


FIG. 18 — FEA model of pure shear specimen: (a) full specimen and (b) quarter model.

Results from high-strain-rate material tension tests up to break on 25 phr carbon black-filled NR were used to develop the hyperviscoelastic constitutive equations and damage initiation. Crack growth in tensile strip and pure shear fracture specimens made with of the same material were then simulated in ABAQUS Explicit. The CZM was successfully able to predict the deformation and crack behavior of these specimens with a very fine mesh near the crack tip and in the crack path. However, adjustments on the critical strain energy density for damage initiation were made to

| ABAQUS solver     | Dynamic, Explicit Version 6.12             |  |
|-------------------|--|--|
| Geometry          | h/2 = 9.5  mm (half length)                |  |
|                   | w = 260.0  mm (width)                      |  |
|                   | t/2 = 0.702 mm (half thickness)            |  |
| Elements          | C3D8, 8-node linear full-integration brick |  |
|                   | No. of elements $= 2448$                   |  |
| Loading type      | 76.2-cm drop height, pure shear            |  |
| Crack parameter m | m=5  |  |
| Step time         | 30 ms                                      |  |
| Run time          | 25 h (4 CPU)                               |  |

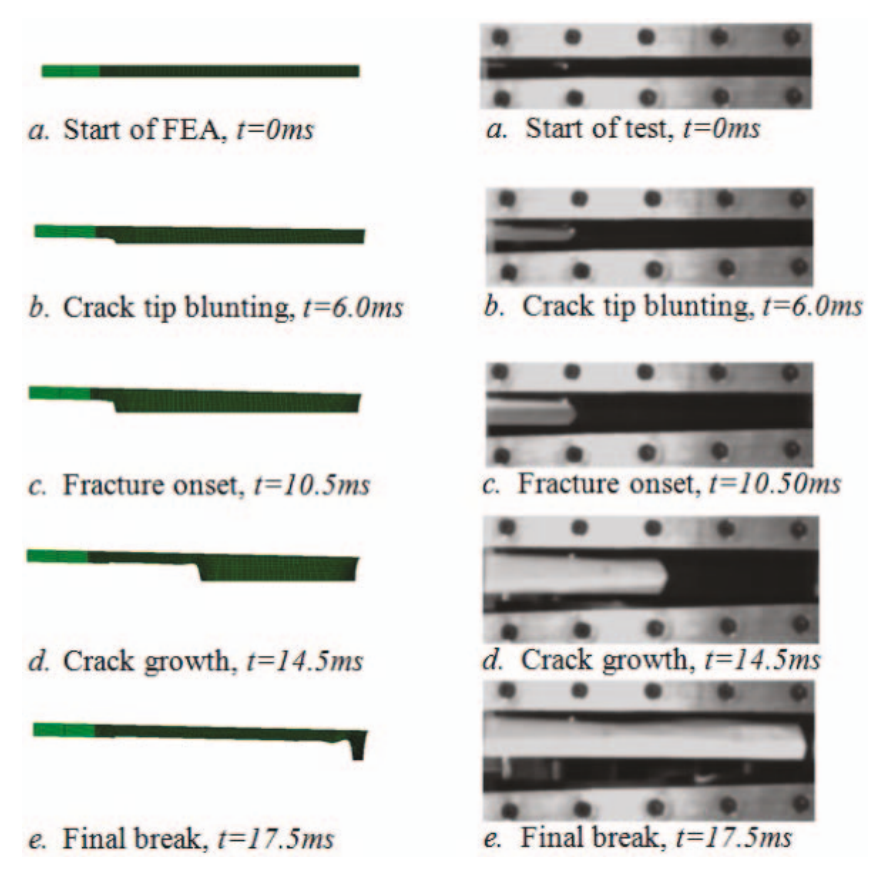


FIG. 19 — Side-by-side comparison of pure shear tearing in FEA and test for 76.2-cm drop height.

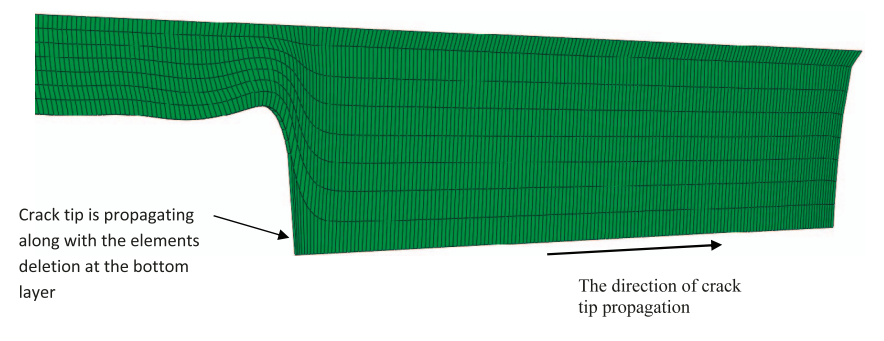


FIG. 20 — Close-up view of crack tip in pure shear specimen during test at 76.2-cm drop height.

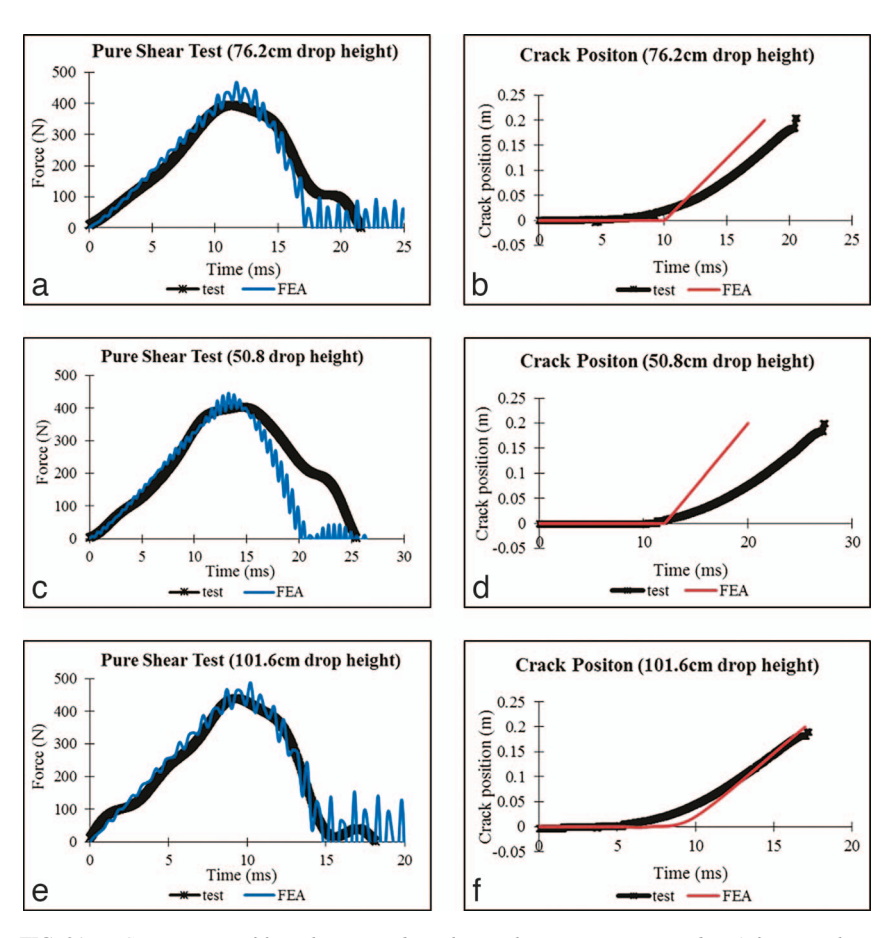


FIG. 21 — Comparisons of force history and crack growth positions in test and FEA for pure shear experiments at drop heights of (a–b) 76.2 cm, (b–d) 50.8 cm, and (e–f) 101.6 cm.

avoid using small elements and long program run times. These adjustments did not affect the overall deformation and crack behavior of these specimens.

## Acknowledgments

This project was funded by CenTire, an NSF I/UCRC. The authors would like to thank their industry mentors within CenTire, who not only supported this project but also provided healthy discussions and advice throughout the research.

#### References

- [1] Griffith, A. A., "The Theory of Rupture," in Biezeno, C. B., and Burgers, J. M. (eds.), *The Proceeding of the First International Congress for Applied Mechanics*, Delft, the Netherlands, 1925, pp. 55–63.
- [2] Rivlin, R. S. and Thomas, A. G., "Rupture of Rubber. I. Characteristic Energy for Tearing," *Journal of Polymer Science*, Vol. 10, 1953, pp. 291–318.
- [3] Thomas, A. G., "Rupture of Rubber. VI. Further Experiments on the Tear Criterion," *Journal of Applied Polymer Science*, Vol. 3, 1960, pp. 168–174.
- [4] Gent, A. N., "Strength of Elastomers," in Mark, J. E., Erman, B., and Eirich, F. R. (eds.), Science and Technology of Rubber, 3rd ed., Elsevier Academic Press, Boston, 2005, pp. 455– 495.
- [5] Previati, G. and Kaliske, M., "Crack Propagation in Pneumatic Tires: Continuum Mechanics and Fracture Mechanics Approaches," *International Journal of Fatigue*, Vol. 37, 2012, pp. 69–78.
- [6] Kroon, M., "Dynamic Steady-State Analysis of Crack Propagation in Rubber-like Solids Using an Extended Finite Element Method," *Computational Mechanics*, Vol. 49, 2012, pp. 73–86.
- [7] Sun, C. T. and Jin, Z. H., Fracture Mechanics, Academic Press, Waltham, MA, 2012.
- [8] Hillerborg, A., Modeerand, M., and Petersson, E., "Analysis of Crack Formation and Crack Growth in Concrete by Means of Fracture Mechanics and Finite Elements," *Cement and Concrete Research*, Vol. 6, 1976, pp. 773–782.
- [9] Xu, X. P. and Needleman, A., "Numerical Simulations of Fast Crack Growth in Brittle Solids," Journal of the Mechanics and Physics of Solids, Vol. 42, 1994, pp. 1397–1434.
- [10] Planas, J. and Elices, M., "Nonlinear Fracture of Cohesive Materials," *International Journal of Fracture*, Vol. 51, 1991, pp. 139–157.
- [11] Rahulkumar, P., Jagota, A., Bennison, S. J., and Saigal, S., "Cohesive Element Modeling Of Viscoelastic Fracture: Application to Peel Testing of Polymers," *International Journal of Solids and Structures*, Vol. 37, 2000, pp. 1873–1897.
- [12] Tijssens, M. G. A., Van Der Giessen, E., and Sluys, L. J., "Modeling of Crazing Using Cohesive Surface Methodology," *Mechanics of Materials*, Vol. 32, 2000, pp. 19–35.
- [13] Spanda, M. and Philippe, H. G., "A Cohesive Model for Fatigue Failure of Polymers," Engineering Fracture Mechanics, Vol. 72, 2005, pp. 691–708.
- [14] De Borst, R., Joris, J. C. R., and Needleman, A., "Mesh-Independent Discrete Numerical Representations of Cohesive-Zone Models," *Engineering Fracture Mechanics*, Vol. 73, 2006, pp. 160–177.
- [15] Elmukashfi, E. and Kroon, M., "Numerical Analysis of Dynamic Crack Propagation in Rubber," *International Journal of Fracture*, Vol. 177, 2012, pp. 163–178.
- [16] Al-Quraishi, A. A. and Hoo Fatt, M. S., "Dynamic Fracture of Natural Rubber," *Tire Science and Technology*, Vol. 35, 2007, pp. 252–275.
- [17] Hoo Fatt, M. S., Chen, L., and Al-Quraishi, A. A., "Fracture Parameters for Natural Rubber under Dynamic Loading," Strain, Vol. 47, 2011, pp. 505–518.
- [18] Bekar, I., Hoo Fatt, M. S., and Padovan, J., "Tensile Impact Apparatus," U.S. Patent 7-320-242, January 22, 2008.
- [19] Kuhn, H. and Medlin, D., "ASM Handbook Mechanical Testing and Evaluation," Materials Park, Vol. 8, 2001.

# 324 TIRE SCIENCE AND TECHNOLOGY

- [20] Mullins, L., "Softening of Rubber by Deformation," Rubber Chemistry and Technology, Vol. 42, 1969, pp. 339–362.
- [21] Huber, N. and Tsakmakis, C., "Finite Deformation Viscoelasticity Laws," *Mech. Mater.* Vol. 32, 2000, pp. 1–18.
- [22] Yeoh, O. H., "Some Forms of the Strain Energy Function for Rubber," *Rubber Chemistry and Technology*, Vol. 66, 1993, pp. 754–771.